Optical Science and its Applications in Industry and Health

Optical Science and its Applications in Industry and Health

By

Dahi Ghareab Abdelsalam Ibrahim

Cambridge
Scholars
Publishing

Optical Science and its Applications in Industry and Health

By Dahi Ghareab Abdelsalam Ibrahim

This book first published 2024

Cambridge Scholars Publishing

Lady Stephenson Library, Newcastle upon Tyne, NE6 2PA, UK

British Library Cataloguing in Publication Data
A catalogue record for this book is available from the British Library

ISBN (10): 1-0364-0697-0
ISBN (13): 978-1-0364-0697-4

TABLE OF CONTENTS

ACKNOWLEDGMENTS

First and foremost, I would like to thank my beautiful wife-to-be for allowing me to spend hours writing and days traveling to become an expert in such an international field – thanks El-Shaimaa. I would also like to thank my mother, my brothers, and my sons Hagar, Hamza, and Youssef. Last, but not least, this book is dedicated to the soul of my father, the one that I want to please the most – thanks, Dad!

Prof.Dr. Dahi Ghareab Abdelsalam Ibrahim
Head of Length and Precision Engineering Division
National Institute of Standards (NIS), Egypt.
2024

CHAPTER ONE

CALIBRATION OF STEP HEIGHTS OPTICALLY

1.1 Introduction

Step height/depth standards are needed for various purposes in length metrology. The control of critical dimensions in the fabrication of micro-electronics and micro-optics, for example, is commonly performed using calibrated step height/depth standards [1-2]. Also, the axial scale of the measuring instruments such as the metrological atomic force microscope (AFM) is calibrated by a calibrated step height standard [3] termed (H800) made of silicon and silicon oxide covered by a metallic layer with a nominal axial step height of 800 nm and a lateral nominal width of 20µm. Step height/depth standards are calibrated optically by fringe evaluation in a calibrated interference microscope with stabilized wavelengths in agreement with the definition of the meter [4-5] through the ISO 5436 profile analysis [6]. As seen in the inset of Fig. 1.1, the ISO 5436 profile analysis for groove structures provides the axial depth measurements of step depth standards by averaging the depths at the active measurement areas at the edges minus the average depth at the active measurement area at the groove. The ISO 5436 profile analysis doesn't provide a direct method for the lateral measurements of the step height/depth standards. Lateral measurements of the step height/depth standards represent the sharpness of the two line edges of the step height/depth standard. Occasionally, the two line edges or one of them may not be sharp enough due to manufacturing defects or overuse. The sharpness of the two line edges of the step height/depth standards is a crucial measure for the evaluation of the mask projection process in lithographic applications [7-8]. In this work, we present a new method based on the Hamming area model for the lateral measurements of a groove structure of a transparent step depth standard. The basic idea of the method is to mimic the experimental profile of the step depth being measured by a combination of the Hamming window: pass-band filter and the root mean square (RMS) model. The lateral position of the 50% depth value of the mimicked Hamming depth is assigned. The areas up and down the assigned value are then computed and compared for the lateral measurements of the step depth standard. The common-path phase-shift microscope based on the measurement of the Stokes parameters S_2 and S_3 [9] is used to extract the experimental profile of the groove structure. The microscope is designed by the author at the National Institute of Standards (NIS) for calibration of transparent step height/depth standards with measured temporal stability down to 1.3 nm. The results show that the total area included in the right line edge of the groove structure is greater than the total area included in the left line edge by 151.66 nm. The difference between the total area included in the right line edge and the total area included in the left line edge or degree of symmetry determines a real lateral measurement of the step depth standard corresponding to the manufacturing defects or erosion due to overuse. A high degree of symmetry means that the line edges of the step depth standard are sharp, while a low degree of symmetry means that the two line edges or one of them are blunt. The error in area measurement is computed to be 1.7%. The proposed method gives a better assessment of the sharpness of the line edges and hence improves the lateral resolution of the measuring instrument. Moreover, it improves the axial height/depth measurements of the structure being measured. The proposed method can be applied to any step height/depth regardless of its height/depth, width, and sharpness of the line edges. Moreover, the method can be used to address the creep problem for a piezo electrical scanning system in the AFM. To the best of our knowledge, this is the

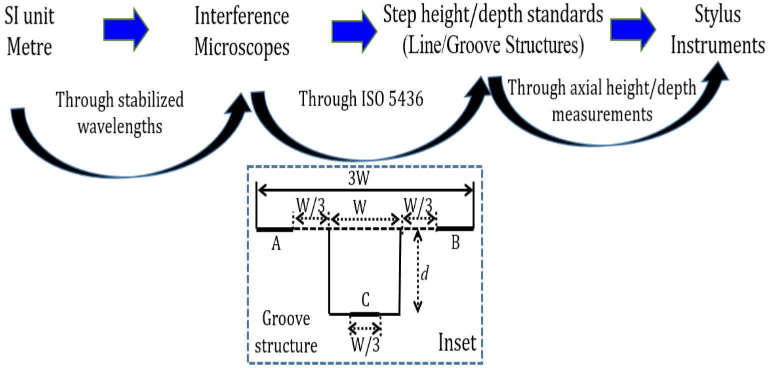

Fig.1.1 Schematic representation of the current calibration of step height standards using ISO 5436 traceable to SI unit. Step height standards stand for line structures, while step depth standards stand for groove structures.

first report of the Hamming area model for lateral measurements of step height/depth standards. The following sections contain the theoretical and experimental descriptions of the lateral measurements of step depth standards by the proposed Hamming area model.

1.2 Hamming Area Model

A window function is used to analyze a small part of a signal. Usually the values of the signal outside the window are zero or rapidly tend to be zero. Some of the windows that are most frequently used are the rectangular window, the Bartlett window, the Gaussian window, the Blackman window, the flat-top window, and the Hamming window. The commonly used window is the Hamming window. The Hamming window can be used as a band-pass filter by multiplying it with a signal in the frequency domain. This effectively removes low-frequency components and high-frequency components, leaving only the frequencies in the desired band. Band-pass filters are used to permit a range of frequencies within a lower and upper threshold. The Hamming window: pass-band filter is expressed as [10-11]:

$$w_H(n) = 0.54 - 0.46\cos\left(\frac{2\pi n}{N-1}\right), \tag{1.1}$$

where $n \in \{0,\ldots, N\text{-}1\}$ and N is the filter order. Figure 1.1(a) shows an example of an original waveform of $y = \sin(2\pi t/100)$ with t = (0: 500). The Hamming window profile of $y = \sin(2\pi t/100)$. * window (@hamming, 501) is shown in Fig. 1.2(b). The discrete-time Fourier transform (DTFT) of the sequence $2h(n)\cos(2\pi n f_0) = h(n)e^{2j\pi n f_0} + h(n)e^{-2j\pi n f_0}$ can be written as $H(f - f_0) + H(f + f_0)$ where h is the impulse response, and f_0 is the cut-off frequency. Here, one component of $H(f - f_0)$ or $H(f + f_0)$ is selected. Hence, if $H(f)$ is the complex gain of a low-pass filter, the result is a filter the complex gain of which is centered around $\pm f_0$, therefore a band-pass filter. In order to maintain a linear phase, a 2 cos $(2\pi n\, f_0)$ is multiplied if N is odd and is multiplied if N is even. For N odd, the impulse response $h(n)$ is expressed as

$$h(n) = \int_{-f_0}^{f_0} e^{2j\pi n f}\,df = \frac{\sin(2\pi n f_0)}{\pi n}, \tag{1.2}$$

and for N even, the impulse response $h(n)$ is expressed as:

$$h(n) = \int_{-f_0}^{f_0} e^{j\pi f} e^{2j\pi n f}\, df = \frac{\sin(2\pi(n+0.5)f_0)}{\pi(n+0.5)}. \tag{1.3}$$

The simulated spectra (abs (2 h(n) cos($2\pi n f_0$)) by the Hamming window: band-pass filter for line structures at $f_0 = 0.25$, $f_b = 0.12$, and $N = 981$, $N = 881$, $N = 781$ are shown in Figs. 1.3(a), 1.3(b), and 1.3(c), respectively.

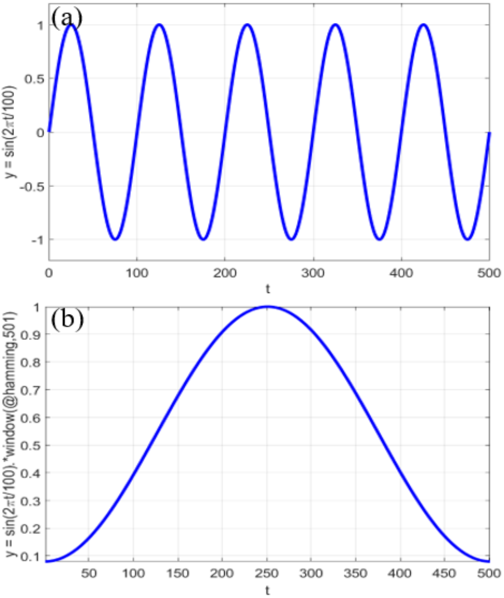

Fig.1.2 (a) Original waveform of $y = \sin(2\pi t/100)$. (b) Hamming window profile of $y = \sin(2\pi t/100)$. * window (@hamming, 501).

Figure 1.3(d) shows a simulated gain spectrum of groove structure with the Hamming window: band-pass filter at cut-off frequency = 0.25, f_b = 0.12, and filter order = 881. As seen in Fig. 1.3, the Hamming window: band-pass filter can mimic line or groove structures regardless of the height, width, and slope of the line edges of the step height just by adjusting the N, f_0, and fb. Here, the f_b is responsible for widening or narrowing the width of the gain. The following procedures should be taken into consideration for accurate lateral measurements of the step height/depth standard being measured. 1- The experimental profile should be mimicked by a combination of the Hamming window: pass-band filter and the RMS model. 2- The gain (vertical axis) of the mimicked profile (as seen in Fig. 1.3, it ranges from 0 to one) should be rescaled to fit the experimental axial scale. Also, the position (horizontal axis) should be rescaled to fit the length (or via the number of pixels) of the horizontal experimental profile. 3- The lateral position of 50% of the height/depth value of the mimicked Hamming height/depth is assigned. 4- The areas up and down the assigned value are computed and compared for the lateral measurements of the step height/depth standard. 5- The differences between the up and down areas of the assigned value are computed for symmetrical determination. Note that, by knowing the differences in areas up and down the assigned value, reconditioning can be implemented for accurate lateral measurements.

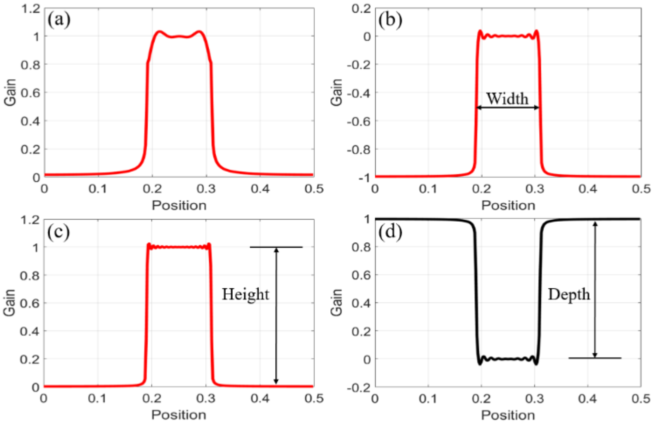

Fig. 1.3 Mimicked spectra of line structures with the Hamming window: band-pass filter at $f_0 = 0.25$, $f_b = 0.12$, and (a) filter order $N = 981$; (b) $N = 881$; and (c) $N = 781$. (d) Mimicked spectrum of groove structure with the Hamming window: band-pass filter at $f_0 = 0.25$, $f_b = 0.12$, and $N = 881$.

1.3 Optical Setup

Figure 1.4 shows the schematic diagram of the optical system used to extract the experimental profile of the object, which is a groove structure of a transparent step depth standard of a nominal axial depth of 60 nm and a lateral nominal width of 200 μm. It is made by plating chrome on a soda-lime glass substrate. The optical system is a common-path phase-shift microscope based on the measurement of the Stokes parameters S_2 and S_3 [9]. Figure 1.4 (a) is used to extract S_{2R} and S_{3R} in the absence of the object, while Fig. 1.4 (b) is used to extract S_{2T} and S_{3T} in the presence of the object. The optical system can be regarded as a combination of Zernike's phase contrast microscopy, which delivers high-contrast intensity images of transparent specimens, and Gabor's holography, where the phase information from the object is recorded. The optical system works by phase shifting technique for precise measurement with an error of $\lambda/100$ [12]. The optical system doesn't employ a PZT phase shifter to avoid the nonlinear response of the PZT to the applied voltage and the thermal drift in the PZT. Moreover, since it is a common-path scheme, it reduces the effects of mechanical vibrations and air turbulence, which are the fundamental error sources in interferometric measurements. The optical system has a measured temporal stability down to 1.3 nm.

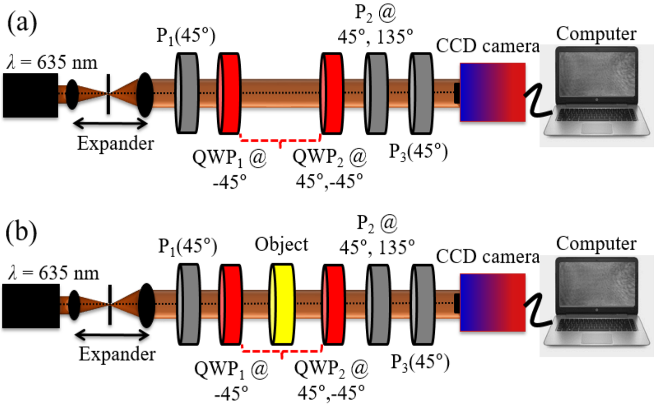

Fig. 1.4 (a) Schematic diagram of the common-path optical phase shift system. P_1 (45°) is a polarizer fixed at 45°; P_2 @ 45°, 135° is a polarizer rotated at 45° and 135° for obtaining the S_{2R} and S_{2T}; QWP$_1$ @ -45° is a quarter wave plate fixed at -45°; QWP$_2$ @ 45°, -45° is a quarter wave plate rotated at 45° and -45° for obtaining the S_{3R} and S_{3T}.

A calibrated laser diode of $\lambda = 635$ nm is connected to a collimation and beam size expansion section which comprises a length extendable tube and a plano-convex lens of 30 mm diameter. A shearing interferometer was used to achieve good collimation. The collimated beam is directed to three polarizers (P_1 (45°), P_2 @ 45°, 135°, P_3 (45°)), two QWPs, the object being measured, and a CCD camera. The three polarizers and the two QWPs were calibrated using a commercial Thorlabs polarimeter. The light is linearly polarized by a polarizer P_1 (set at an azimuth angle $\theta = 45°$). The linear polarized light passes through a QWP$_1$ (set at an azimuth angle $\theta = -45°$). The beam after passing the object, a part of the light remains unscattered and forms a uniform background of the image; the other part is scattered and contains the fine structure information of the object. To extract the phase image of the object (Δ_{Obj}), a reference phase image (Δ_{Ref}) in the absence of the object is extracted and then subtracted from the total phase image (Δ_T) in the presence of the object. To extract (Δ_{Ref}) and (Δ_T), the S_{2R}, S_{2T}, S_{3R}, and S_{3T} should be computed.

The S_{2R} and S_{2T} in the absence and in the presence of the object being measured are computed with no use of QWP_2, and by rotating the polarizer P_2 at 45° and 135°, the intensity images I_{45T} and I_{135T} are captured by the CCD camera. The difference between the two intensity images in the absence of the object is $S_{2R} = (I_{45R} - I_{135R})$. In the same manner, the difference between the two intensity images in the presence of the object is $S_{2T} = (I_{45T} - I_{135T})$.

The S_{3R} and S_{3T} in the absence and in the presence of the object being measured are computed using the QWP_2, keeping the polarizer P_2 fixed at 45°, like P_1 and P_3. By rotating the QWP_2 at 45° (RHC) and −45° (LHC), two intensity images, I_{LHC} and I_{RHC}, are captured by the CCD camera. The difference between the two intensity images in the absence of the object is $S_{3R} = (I_{LHCR} - I_{RHCR})$. The difference between the two intensity images in the presence of the object is $S_{3T} = (I_{LHCT} - I_{RHCT})$. Here, the subletter T in S_{2T} and S_{3T} stands for total and the subletter R in S_{2R} and S_{3R} stands for reference. Also, the subletters RHC stand for Right Hand Circle, and the subletters LHC stand for Left Hand Circle.

The reference phase image (Δ_{Ref}) is computed from the S_{2R} and S_{3R} as follows [9]:

$$\Delta_{Ref} = \tan^{-1}\left(-S_{3R}/S_{2R}\right). \tag{1.4}$$

The total phase image (Δ_T) which includes the reference phase (Δ_{Ref}) and the object phase (Δ_{Obj}) is computed from the S_{2T} and S_{3T} as:

$$\Delta_T = \tan^{-1}\left(-S_{3T}/S_{2T}\right). \tag{1.5}$$

The phase image of the object (Δ_{Obj}) is computed via subtraction of the reference phase (Δ_{Ref}) from the total phase (Δ_T) as:

$$\Delta_{Obj} = \Delta_T - \Delta_{Ref}. \tag{1.6}$$

Figure 1.5 (a) shows the reconstructed phase image of the groove structure of a transparent step depth standard of a nominal depth of 60 nm and a lateral nominal width of 200 µm using Eq. 1.6 after unwrapping using the graph cuts method [13]. A cut line along the blue line of Fig. 1.5 (a) is extracted and shown in the blue phase profile in Fig. 1.5 (b). Note that the experimental phase profile occupies a horizontal distance of 70 pixels in the y direction, so the mimicked Hamming profile should be rescaled to fit the experimental horizontal distance.

1.4 Depth measurement of the groove structure using ISO 5436

The experimental profile is divided into five regions as shown in Fig. 1.5 (b). According to the ISO 5436 profile analysis [9], the height/depth measurements are computed using regions 1, 3, and 5 by averaging the heights/depths at the active measurement areas 1 and 5 minus the average height/depth at the active measurement area 3. Since the ISO 5436 profile analysis doesn't present a method for lateral measurements of step height/depth standards, the Hamming area model is proposed in this article to measure the lateral measurements using regions 2 and 4. As seen in Fig. 1.5 (b), the noise vibration in the phase profiles of regions 1, 3, and 5 varies like a sinusoidal function; thus, phase error (p_{rms}) can be expressed as the root mean square (RMS) value of the disturbed phase. The RMS phase error can be expressed as:

$$p_{rms} = \sqrt{\left[p - \overline{p}\right]^2 / (\aleph - 1)}, \qquad (1.7)$$

where p stands for the phase distribution, $\overline{p}$ denotes the mean values, and $\aleph$ represents the pixel number of the experimental profile. The modified blue profile by applying the RMS model is shown in the red profile in Fig.1.5 (b).

The standard deviation is used to quantify the error before and after applying the RMS model. The raw phase profiles (blue color) of regions 1, 5, and 3 in Fig. 1.5 (b) and their modifications (red color) by the RMS model are shown in Figs. 1.6 (a), (b), and (c), respectively. The standard deviation of the blue profile in Fig. 1.6 (a) is calculated to be $\sigma_{\mathrm{Raw}} = 0.072$ rad, while the standard deviation of the red profile is calculated to be $\sigma_{\mathrm{RMS}} = 0.003$ rad. The difference between σ_{Raw} and σ_{RMS} in Fig. 1.6 (a) is calculated to be $\sigma_{\mathrm{diff}} = 0.072 - 0.003 = 0.069$ rad i.e. depth error = $(0.069 \times 635)/(2\pi) \triangleq 7$ nm. In the same manner, the standard deviation of the blue

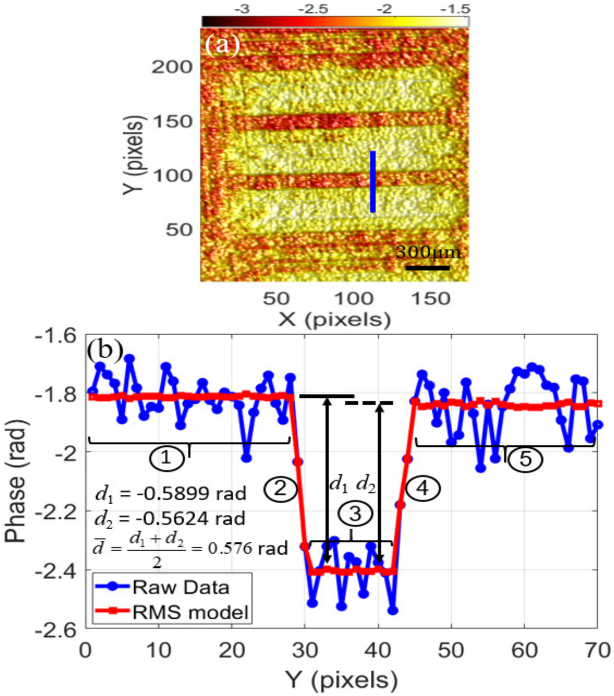

Fig. 1.5 (a) Reconstructed phase image of the groove structure using Eq. 1.6 (b) Experimental phase profile (blue) along the blue line of (a) before applying the RMS model and after applying the RMS model (red profile).

profile in Fig. 1.6 (b) is calculated to be σ_{Raw} = 0.103 rad, while the standard deviation of the red profile in Fig. 1.6 (b) is calculated to be σ_{RMS} = 0.007 rad. The difference between σ_{Raw} and σ_{RMS} in Fig. 1.6 (b) is calculated to be σ_{diff} = 0.103 - 0.007 = 0.096 rad i.e. depth error = (0.096 x 635)/(2pi) ≅ 10 nm.

In the same manner, the standard deviation of the blue profile in Fig. 1.6 (c) is calculated to be σ_{Raw} = 0.085 rad, while the standard deviation of the red profile in Fig. 1.6 (c) is calculated to be σ_{RMS} = 0.004 rad. The difference between σ_{Raw} and σ_{RMS} in Fig. 1.6 (c) is calculated to be σ_{diff} = 0.085 - 0.004 = 0.081 rad i.e. depth error = (0.081 x 635)/(2pi) ≅ 8 nm. Note that the depth measurements have been carried out using the red profiles of Fig. 1.5 (b) i.e. after applying the RMS model. The average standard deviation of the red profiles in regions 1, 5, and 3 is computed to be around 0.4nm. Note also that the measurement noise is found experimentally to be around 0.07nm for one-second data acquisition using a surface topography repeatability test. As seen in Fig. 1.5 (b), the average phase is calculated to be 0.576 rad i.e. depth = (0.576 x 635)/(2pi) ≌ 58.3 nm. The sources of uncertainty [14-15] including the above-measured errors in addition to errors arising from the calibrated laser source and collimation have been estimated to be 0.6 nm, which is about 1% of the measured depth. Note that, by using the Hamming profile, the depth measurement is improved to be 0.589 rad i.e. depth = (0.589 x 635)/(2pi) ≌ 59.7 nm, which approaches the nominal value, which is 60 nm.

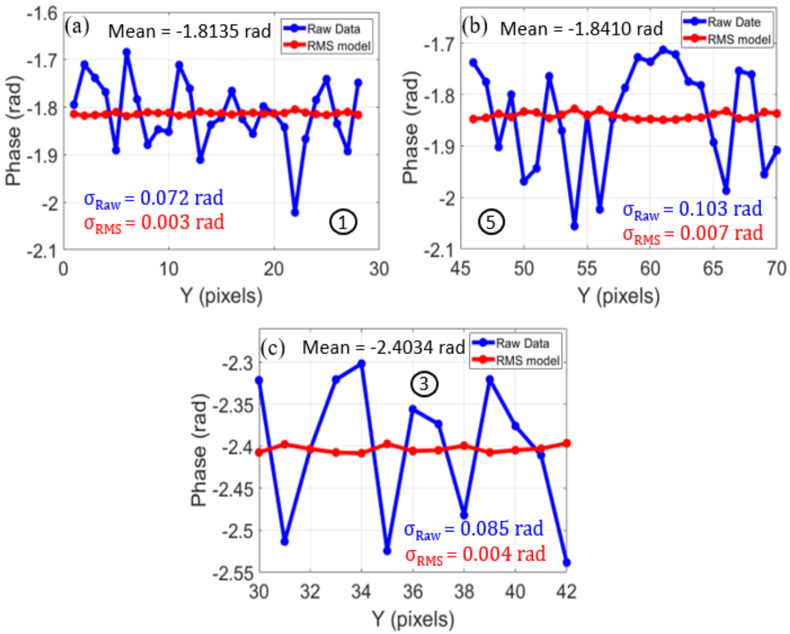

Fig. 1.6 Phase profiles of areas (a) 1, (b) 5, and (c) 3 in Fig. 1.5 (b).

1.5 Lateral measurements of the groove structure using Hamming Area model

The red profile in Fig. 1.7 shows the experimental phase profile after applying the RMS model, while the green color is the mimicked Hamming profile simulated at f_0 = 0.26, f_b = 0.102, and N = 781. The Hamming horizontal axis in Fig.1.7 is rescaled by multiplying a value of 140 to fit the scale of the experimental profile, while the Hamming vertical axis is rescaled by multiplying a value of 0.59 and the result is subtracted from 1.81 value to fit the experimental vertical scale. Note that the mimicked profile is adjusted on the experimental profile after applying the RMS not on the raw profile, which means better accuracy is achieved. As seen in Fig. 1.7, the sharpness of lateral measurements of the left line edge and right line edge is estimated via the Hamming area. We used the expression of Hamming area since the area is computed using the position of the 50% depth value ($0.5d_{\text{Ham}}$) of the mimicked Hamming profile. As seen in Fig. 1.7, the left line edge includes two areas A_1 and A_2, and the right line edge includes two areas A_3 and A_4. The tips of A_1 and A_4 are down, while the tips of A_2 and A_3 are up.

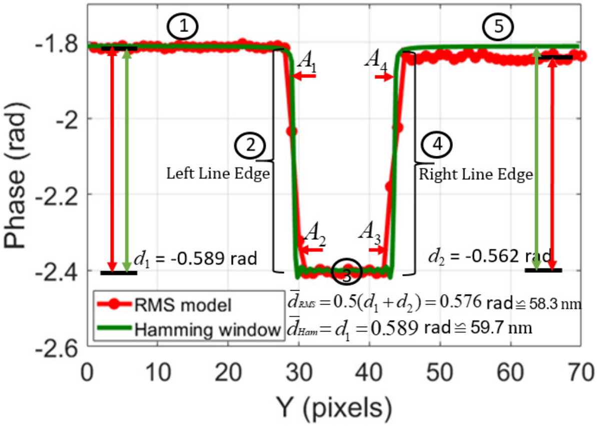

Fig. 1.7 Experimental phase profile (red color) after applying the RMS model, and its mimicked Hamming profile (green color).

Since the two areas (A_1 and A_4) and the two areas (A_2 and A_3) have the same axial depth scale with different lateral spacing, it is more logical to compute the areas of them and compare them to find the difference or degree of symmetry. Alternatively, the two areas of the left line edge A_1 and A_2 are summed up and the result of summation is subtracted from the result of summation of the two areas of the right line edge A_3 and A_4. By knowing the difference, a quantitative lateral reconditioning could be performed.

The first attempt to determine the borders of (A_1 and A_4) and (A_2 and A_3) is to use a fill function in MATLAB to fill the corresponding two areas individually with a specified color. Figure 1.8 (a), for example, shows the experimental profile filled with red color is plotted first, and then the mimicked Hamming profile filled with green color is plotted next. The difference between the two experimental and mimicked Hamming profiles shows only the appearance of the up areas A_1 and A_4 above the $0.5d_{\mathrm{Ham}}$. In the same manner, Fig. 1.8 (b) shows the mimicked Hamming profile filled with red color is plotted first, and then the experimental profile filled with green color is plotted next. The difference between the two mimicked Hamming and experimental profiles shows only the appearance of the down areas A_2 and A_3 below the $0.5d_{\mathrm{Ham}}$.

As seen in Fig. 1.8 (a), the upper borders of area A_4, for example, are not perfectly performed with the intersection of the mimicked Hamming profile (there is a gap between the experimental and its mimicked Hamming profiles), so the convenient solution is to shade the difference in area between the experimental and its mimicked Hamming profiles. Figure 1.9 shows the shaded areas between the experimental and its mimicked profiles using a fill function in MATLAB. As seen in Fig. 1.9, the four lateral areas A_1, A_2, A_3, and A_4 of the left line edge and the right line edge of the groove structure appear clearly with formed borders and with an assigned depth value of $0.5d_{\mathrm{Ham}}$. The assigned point value $0.5d_{\mathrm{Ham}}$ is expressed as:

$$0.5d_{Ham} = (d_0 + d_{Ham}/2) \tag{1.8}$$

The value of d_0 is the average depth at the mimicked edges of regions 1 and 5. The value of d_0 is found to be -1.8135 in Fig. 1.9, and $d_{\mathrm{Ham}}/2 = 0.5899/2 = 0.295$ rad. The assigned value $0.5d_{\mathrm{Ham}} = -1.8135 - 0.2950 = -2.1085$ rad.

As seen in Fig. 1.8 and Fig. 1.9, one can estimate by the naked eye that $A_4 > A_1$ and $A_3 > A_2$ or $|A_3 + A_4| > |A_1 + A_2|$, which means that reconditioning process should be implemented on the right line edge to achieve symmetrical line edges of the groove structure. To quantify this value, the areas A_1, A_2, A_3, and A_4 should be computed precisely.

The integrals of the shaded areas A_1 and A_2 of the left line edge up and down the assigned value of Fig. 1.9 are given as follows:

$$A_1 = \int_{y_1}^{y_2} [d_{Exp}(y) - d_{Ham}(y)]dy, \tag{1.9}$$

$$A_2 = \int_{y_2}^{y_3} [d_{Exp}(y) - d_{Ham}(y)]dy. \tag{1.10}$$

The total area of the left line edge in Fig. 1.9 is expressed as:

$$^{Left\ Line\ Edge}A_T = \left|A_1 + A_2\right|. \tag{1.11}$$

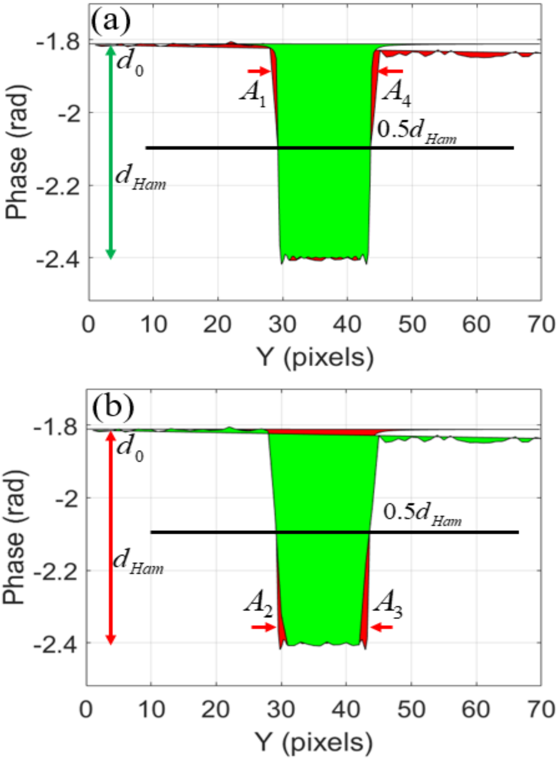

Fig. 1.8 (a) Appearance of the up areas A_1 and A_4 only above the $0.5d_{\mathrm{Ham}}$. (b) The appearance of the down areas A_2 and A_3 only below the $0.5d_{\mathrm{Ham}}$.

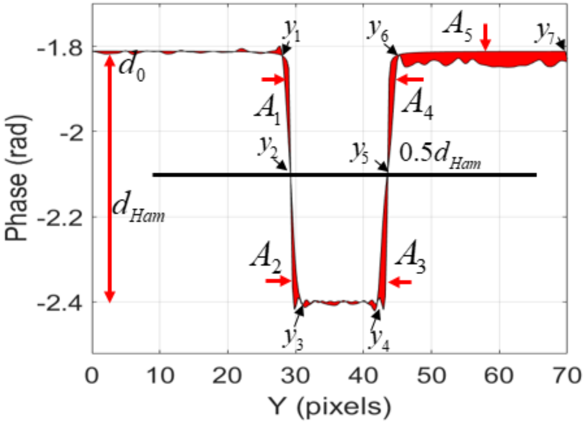

Fig. 1.9 (a) Shaded areas between the experimental and its mimicked Hamming profiles using a fill function in MATLAB. Appearance of the up and down areas A_1, A_2, A_3, and A_4 for lateral measurements.

In the same manner, the integrals of the shaded areas A_3 and A_4 of the right line edge down and up the assigned value of Fig. 1.9 are given as follows:

$$A_3 = \int_{y_4}^{y_5} [d_{Exp}(y) - d_{Ham}(y)]dy, \tag{1.12}$$

$$A_4 = \int_{y_5}^{y_6} [d_{Exp}(y) - d_{Ham}(y)]dy. \tag{1.13}$$

The total area of the right line edge in Fig. 1.9 is expressed as:

$$^{Right\ Line\ Edge}A_T = |A_3 + A_4|. \tag{1.14}$$

The difference (degree of symmetry) between the total area included in the right line edge and the total area included in the left line edge is expressed as:

$$\Delta A = {}^{Right\ Line\ Edge}A_T - {}^{Left\ Line\ Edge}A_T. \tag{1.15}$$

Here, we used the trapz function in MATLAB to integrate the data with unit spacing. The function trapz performs the numerical integration via the trapezoidal method. This method approximates the integration over an interval by breaking the area down into trapezoids with more easily computable areas.

For an integration with S+1 evenly–spaced points, the approximate is expressed as follows [16]:

$$\int_a^b f(y)dy \approx \frac{b-a}{2S}\sum_{n=1}^{S}\left(f(y_n)+f(y_{n+1})\right), \tag{1.16}$$

where the spacing between each point is equal to the scalar value (b-a)/S. By default, MATLAB uses a spacing of 1. If the spacing between the S+1 points is not constant, then the formula generalizes to the following equation:

$$\int_a^b f(y)dy = \frac{1}{2}\sum_{n=1}^{S}\left(y_{n+1}-y_n\right)\left[f(y_n)+f(y_{n+1})\right], \tag{1.17}$$

where $a = y_1 < y_2 <\ldots< y_S < y_{S+1} = b$, and ($y_{n+1}$- y_n) is the spacing between each consecutive pair of points.

As seen in Fig. 1.10 (a) and Fig. 1.10 (b), a trapezoidal integration of A_1 in Fig. 1.9 was computed using thirteen evenly-spaced trapezoids, while a trapezoidal integration of A_2 was computed using seventeen evenly-spaced trapezoids.

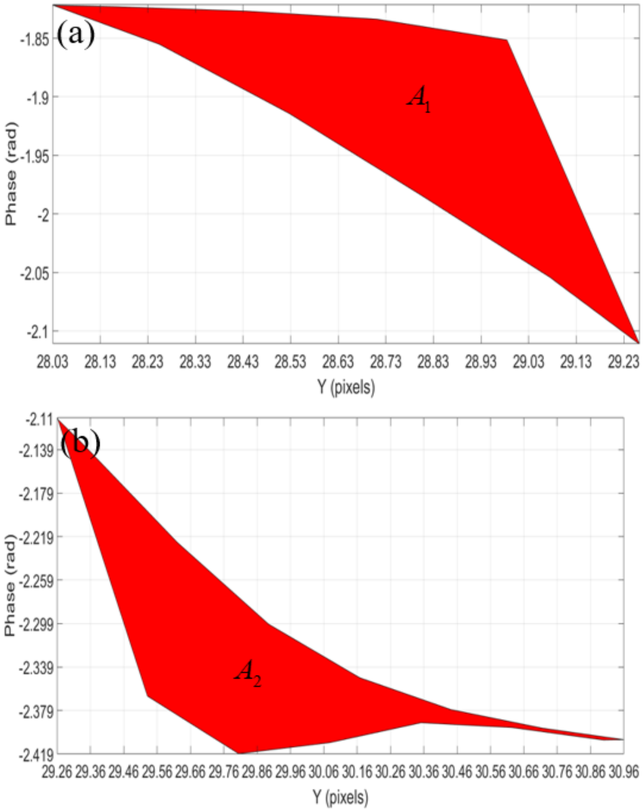

Fig. 1.10. (a) Area 1 (A_1) in Fig. 1.9 with thirteen evenly-spaced trapezoids. (b) Area 2 (A_2) in Fig. 1.9 with seventeen evenly-spaced trapezoids.

As seen in Fig. 1.11 (a) and Fig. 1.11 (b), a trapezoidal integration of A_3 in Fig. 1.9 was computed using sixteen evenly-spaced trapezoids, while a trapezoidal integration of A_4 was computed using seventeen evenly-spaced trapezoids.

The approximate integrations of the four lateral areas A_1, A_2, A_3, and A_4 using the trapz function in MATLAB yield values of -1.044 rad, -1.086 rad, -2.09 rad, and -1.54 rad, respectively. The total area included in the left line edge is computed using Eq. 1.11 to be: $|A_1+A_1| = |-1.044-1.086| = |-2.13| = 2.13$rad. Also, the total area included in the right line edge is computed using Eq. 1.14 to be: $|A_3+A_4| = |-2.09-1.54| = |-3.63| = 3.63$rad. The difference (degree of symmetry) between the total area included in the right line edge and the total area included in the left line edge is computed using Eq. 1.15 to be: ΔA = 3.63 rad – 2.13 rad = 1.5 rad = (1.5 x 635/2 x π) = 151.66nm.

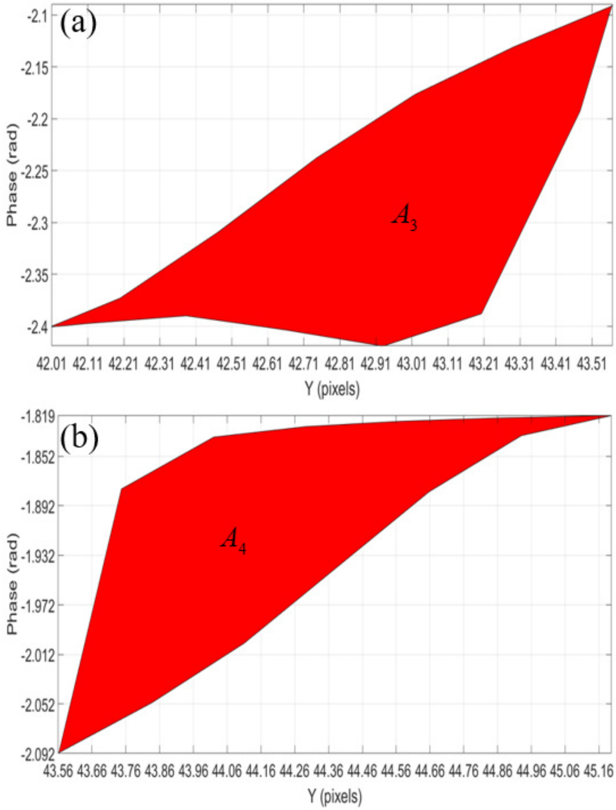

Fig. 1.11 (a) Area 3 (A_3) in Fig. 1.9 with sixteen evenly-spaced trapezoids. (b) Area 4 (A_4) in Fig. 1.9 with seventeen evenly-spaced trapezoids.

This means that a reconditioning process should be applied to remove 151.66 nm from the right line edge to be symmetrical with the left line edge. More specifically, the value of 151.66 nm is distributed over the two included areas A_3 and A_4 in the right line edge as follows: the absolute difference in up areas A_1 and A_4 above the $0.5d_{\mathrm{Ham}}$ is expressed as $|A_4\text{-}A_1|$ = $|-1.54+1.044|$ = 0.496 rad = = (0.496 x 635/2 x π) = 50.15 nm. In the same manner, the absolute difference in down areas A_2 and A_3 below the $0.5d_{\mathrm{Ham}}$ is expressed as $|A_3\text{-}A_2|$ = $|-2.09+1.086|$ = 1.004 rad = = (1.004 x 635/2 x π)

= 101.51 nm. This means that the reconditioning process should be applied to remove 50.15 nm from A_4 and remove 101.51 nm from A_3 to be symmetrical with the areas A_1 and A_2, respectively. The error in area measurement by the trapz function was estimated by applying the trapz function to compute many simulated standard areas. For example, a standard area of 42 was computed by the trapz function to be 41.3, i.e. the error in area measurement is 1.7%. Table 1.1 shows the obtained results of areas A_1, A_2, A_3, and A_4 of the groove structure computed with the trapz function.

Left Line Edge		Right Line Edge	
Area	Computed value (rad)	Area	Computed value (rad)
A_1	-1.044	A_3	-2.09
A_2	-1.086	A_4	-1.54
$\|A_1 + A_2\|$	2.13	$\|A_3 + A_4\|$	3.63
$\Delta A = \|A_3 + A_4\| - \|A_1 + A_2\| = 3.63$ rad – 2.13 rad = 1.5 rad = (1.5 x 635/2 x π) = 151.66 nm			

Table 1.1 Measurement of areas A_1, A_2, A_3, and A_4 of the groove structure.

1.6 Discussion

The benefits of using the mimicked Hamming profile are not only in the lateral measurements of the groove structure by the Hamming area model but also in the improvement of the axial measurements. The evidence of the improvement of the axial measurements by the mimicked Hamming profile. Without using the mimicked Hamming profile, the average measured depth was computed to be 58.3 nm as shown in Fig. 1.5 (b). However, by using the mimicked Hamming profile, the average depth was computed to be 59.7 nm as shown in Fig. 1.7. The computed depth value approaches very closely to the nominal depth value of the transparent depth standard, which is 60 nm. This means that by using the mimicked Hamming profile, the depth measurement is improved by around 2.3%.

The mimicked Hamming profile can be used to address the creep problem for a piezo electrical scanning system in AFM. Figure 1.12 shows a groove structure of a nominal standard depth of 350 nm. As seen in the blue profile of Fig. 1.12, there is a problem to achieve precise measurements at the edges of the profile due to the creep problem in a piezo electrical scanning system of the AFM. This problem is solved by the mimicked Hamming profile as seen in the green profile of Fig. 1.12. The Hamming profile is mimicked at cut-off frequency = 0.24, $f_b = 0.39$, and filter order = 881. The Hamming vertical axis is rescaled by multiplying a value of 360 and the result is added to a value of 100 to fit the experimental vertical scale.

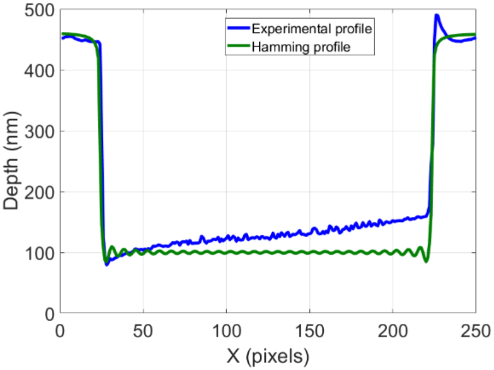

Fig. 1.12 Experimental phase profile (blue color) measured by the AFM, and its mimicked Hamming profile (green color).

In conclusion, we have presented a new method based on the Hamming area model for precise lateral measurements of the line/groove structures. The lateral measurements of the step height/depth standards are a crucial measure for the evaluation of the mask projection process in lithographic applications. The method improves the axial measurements of the line/groove structures by around 2.3%. Moreover, it is used to address the creep problem of a piezo electrical scanning system in AFM. Since the ISO 5436 profile analysis doesn't present a direct method for the lateral measurements of the line/groove structures, we claim that the proposed Hamming area model for precise lateral measurements should be added to the ISO 5436 for axial and lateral step height/depth calibrations.

References

1. Peter J. de Groot, "The meaning and measure of vertical resolution in optical surface topography measurement", Applied Sciences, 7, 54, 2- 6, 2017.

2. ISO DIS 25178-600:201: Geometrical Product Specifications (GPS)-Surface Texture: Areal-Part 600: Metrological Characteristics for Areal-Topography Measuring Methods (DRAFT 2016-05-07); International Organization for Standardization: Geneva, Switzerland, 2016.
3. J. Garnaes, N. Kofod, A. Kühle, C. Nielsen, K. Dirscherl, L. Blunt, "Calibration of step heights and roughness measurements with atomic force microscopes," Precision Engineering, 27, 91-98, 2003.
4. Dahi Ghareab Abdelsalam Ibrahim, T. Yasui, "Multi-object investigation using two-wavelength phase-shift interferometry guided by optical frequency comb," Applied Physics Letters, 112, 171101-171104, 2018.
5. Dahi Ghareab Abdelsalam Ibrahim, T. Yasui, "High-precision 3-D surface topography measurement using high-stable multi-wavelength digital holography referenced by optical frequency comb", Optics Letters, 43, 1- 4, 2018.
6. ISO/TC 213, "Geometrical product specifications (GPS) – Surface texture: Profile method; Measurement standards - Part 2: Software measurement standards," ISO 5436, Edition: 2, Number of pages: 17, 2012.
7. Dahi Ghareab Abdelsalam Ibrahim, "Improving the intensity-contrast image of a noisy digital hologram by convolution of Chebyshev type 2 and elliptic filters", Appl. Opt. 60, 3823-3892, 2021.
8. Dahi Ghareab Abdelsalam Ibrahim, "Enhancement of the steepness measurement of a film thickness edge using wavelet transforms with fringe thinning," OSA Continuum, 3, 1928-1937, 2020.
9. Dahi Ghareab Abdelsalam Ibrahim, "Common-path phase-shift microscope based on measurement of Stokes parameters S_2 and S_3 for 3D phase extraction", Appl. Opt. 59, 5779-5784, 2020.
10. Dahi Ghareab Abdelsalam Ibrahim, "Calibration of a step height standard for dimensional metrology using phase-shift interferometry and Hamming window: band-pass filter," J Opt. 1-9, 2023.
11. Gerard Blanchet, Maurice Charbit, "Digital signal and image processing using MATLAB," John Wiley & Sons, Inc., 2nd Edition, Volume 2, ISBN 978-1-84821-640-2, ISTE Ltd, 2014.
12. Y.-Y. Cheng and J. C. Wyant, "Two-wavelength phase-shifting interferometry," Appl. Opt. 23, 4539,1984.
13. J. M. Bioucas-Dias and G. Valadão, "Phase unwrapping via graph cuts," IEEE Trans. Image Process. 16, 698–709, 2007.
14. JCGM 100:2008 Evaluation of Measurement Data-Guide to the Expression of Uncertainty in Measurement (GUM); Joint Committee for Guides in Metrology: Geneva, Switzerland, 2008.

15. Dahi Ghareab Abdelsalam Ibrahim, “Estimation of an uncertainty budget and performance measurement for a dual-wavelength Twyman-Green interferometer,” J Microsc. 282, 1-15, 2021.

CHAPTER TWO

DETECTION OF DEFORMED BIOLOGICAL CELLS

Optical science plays an important role in health. We present a review of the new frontier of optical science in health focusing on recent optical techniques, and reconstruction methods for accurate biological cell deformation measurement. First, the detection of deformed biological cells irradiated by ionizing radiations is explained. Then we describe the use of spatial light modulators in discrimination between cancerous and normal cells. Method of quantitative phase imaging for 3D deformed cell extraction is also provided.

2.1 Detection of deformed biological cells irradiated by ionizing radiations

Cancer cells grow and divide faster than most normal cells [1-2]. Radiation therapy utilizes high-energy rays, such as x-rays and gamma rays to destroy the cancer cells [3-4]. Radiation works by making small breaks in the DNA inside cells. These breaks keep cancer cells from growing and dividing and cause them to die. Nearby normal cells can also be affected by radiation. The effects can be viewed in the increased number of cells in the deformation of the boundaries of the cells or in both [5-6]. Since there are many factors that can increase the number of red blood cells (RBCs) other than radiation [7], thus counting the number of cells method may be not the correct choice for a perfect diagnosis of the disease. In this paper, we propose to measure the deformation of the red blood cells (RBCs) boundaries, instead of counting the number of RBCs method, to detect the disease in its early stages. A digital bio-dosimeter with a square window size of 7 x 7 pixels is proposed for the quantitative detection of such deformation. The basic idea of the digital bio-dosimeter is to compute the whole energy of the window size of the bio-dosimeter by calculating the summation of the entire gray levels inside the area of the window size [8]. The boundary deformations of the cells can be classified into boundary irregularities and boundary erosions. In this study, male